



OPEN ACCESS

EDITED BY

Fei Wang,
Qingdao University of Science and
Technology, China

REVIEWED BY

Zhengzheng Cao,
Henan Polytechnic University, China
Xiong Yixue,
Chongqing University of Science and
Technology, China

*CORRESPONDENCE

Qiantao Jiang,
✉ jiangqt1010@163.com

RECEIVED 17 November 2025

REVISED 11 February 2026

ACCEPTED 02 March 2026

PUBLISHED 02 April 2026

CITATION

Jiang Q (2026) Multiscale
characterization of pore–throat
structures and flow mechanisms in
low-permeability reservoirs.
Front. Earth Sci. 14:1748091.
doi: 10.3389/feart.2026.1748091

COPYRIGHT

© 2026 Jiang. This is an open-access
article distributed under the terms of
the [Creative Commons Attribution
License \(CC BY\)](https://creativecommons.org/licenses/by/4.0/). The use, distribution or
reproduction in other forums is
permitted, provided the original
author(s) and the copyright owner(s) are
credited and that the original
publication in this journal is cited, in
accordance with accepted academic
practice. No use, distribution or
reproduction is permitted which does
not comply with these terms.

Multiscale characterization of pore–throat structures and flow mechanisms in low-permeability reservoirs

Qiantao Jiang*

Shenzhen Branch of CNOOC (China) Co., Ltd., Shenzhen, Guangdong, China

Introduction: The study focuses on the characterization of pore–throat structures and flow mechanisms in low-permeability reservoirs. Due to complex microstructures and unclear non-linear flow behaviors, understanding and accurately modeling the relationship between pore structures and macroscopic flow characteristics is crucial for effective reservoir evaluation.

Methods: A comprehensive approach combining macroscopic physical property testing, microscopic pore–throat characterization, and digital rock simulation was adopted. Techniques such as mercury injection, nuclear magnetic resonance (NMR), and X-ray CT scanning were used for pore structure analysis, while lattice Boltzmann method (LBM) simulations were employed for flow behavior evaluation.

Results: The study reveals distinct differences in pore structure between the W1 and W2 blocks of the Weixinan Sag. The W1 block has well-connected intergranular dissolution pores, while the W2 block contains smaller intercrystalline pores with stronger adsorption effects, leading to reduced flow capacity. The results also show a clear relationship between microstructure and macroscopic flow behavior, with the W1 block showing better flow potential.

Discussion: The findings suggest that traditional reservoir classification methods may not sufficiently account for the complexities of low-permeability reservoirs. This study introduces a multi-parameter classification system based on pore–throat topology and non-Darcy flow characteristics, which can better predict high-quality reservoirs and guide differentiated development strategies.

KEYWORDS

digital core, low permeability reservoir, multi-scale pore structure, non-Darcy flow, reservoir classification system

1 Introduction

With the gradual expansion of global oil and gas exploration into unconventional domains, difficult-to-produce reserves, represented by tight sandstone and sandy conglomerate, have become a crucial position for energy succession (Huang et al., 2022). However, compared with conventional reservoirs, these low-porosity and low-permeability reservoirs have undergone intense diagenetic alteration. They generally exhibit characteristics of complex pore structures, strong heterogeneity, and flow

channels that present micro-to nano-scale multiscale coupling. This complex microscopic topological structure causes the fluid transport behavior in porous media to deviate significantly from the traditional linear Darcy's law. Therefore, accurately characterizing the microscopic pore structure and revealing its control mechanism on macroscopic seepage behavior has become a key scientific issue for reservoir classification evaluation and the prediction of high-quality reservoirs.

The characterization of low-permeability reservoirs plays a pivotal role in the oil and gas industry. Through fine characterization of these reservoirs, reservoir and fluid properties can be better understood, thereby optimizing production schemes and enhancing hydrocarbon recovery (Zhang et al., 2025). Low-permeability reservoir characterization involves various aspects, including pore characterization (Zhao et al., 2017; Lai et al., 2023) and permeability determination. Pore characterization techniques range from conventional core analysis and scanning electron microscopy (SEM) to numerical simulation and digital rock technologies. In the field of pore structure characterization, Lai et al. (Gong and Bai, 2024) pointed out that the formation of deep high-quality clastic reservoirs is dually controlled by sedimentary and diagenetic environments; consequently, traditional single experimental methods struggle to balance the field of view with resolution, necessitating the establishment of an integrated "macro-micro" genetic evaluation system. On this basis, Gong et al. (Lin et al., 2025) quantitatively characterized tight sandstones in the Ordos Basin using fractal theory. Regarding the mechanical response and energy evolution of complex rock structures, Lin et al. (Chi et al., 2024) further investigated the energy evolution mechanism and fractal characteristics of rock failure under dynamic loading, providing a new perspective for understanding the structural stability of complex porous media under stress. The multi-scale fusion method proposed by Chi et al. (Wang et al., 2025), combined with an attention mechanism, achieved hierarchical identification of intergranular pores and clay micro-pores in sandstone, offering a new approach for pore-throat distribution modeling. Additionally, Wang et al. (Faramarzi-Palanger and Mirzaei-Paiaman, 2021) utilized high-pressure mercury injection (HPMI) experiments to obtain capillary pressure curves, which, when combined with NMR T_2 spectra, further inverted the pore-throat diameter distribution and corresponding permeability contributions, validating the quantitative relationship between pore throats and irreducible water saturation. Faramarzi-Palanger et al. (Cheng et al., 2024) applied the TEM-Function dynamic rock typing method to integrate porosity, absolute permeability, and relative permeability into an evaluation system, achieving the classification of flow dynamic rock types and providing a theoretical and practical basis for reservoir classification.

In terms of microscopic flow mechanisms and numerical simulation, the linear assumption under traditional Darcy flow conditions is no longer applicable in low-permeability reservoirs, necessitating the introduction of non-Darcy flow and threshold pressure gradient (TPG) models. Cheng et al. (Yunlong et al., 2024) reviewed the pre-Darcy flow theory, pointing out the non-linear relationship between flow velocity and pressure difference under low pressure gradients, which requires precise quantification through microscopic flow experiments. The TPG of low-permeability reservoirs is not a constant value but follows a power-law variation with permeability and fluid properties. Jia

et al. (Zhengzheng et al., 2024) proposed the non-linear evolution characteristics and a seepage mechanical model of fluids in broken rock mass based on the bifurcation theory, which greatly enriched the theoretical framework of non-Darcy flow. Furthermore, the application of numerical simulation methods has extended to complex fluid–solid coupling problems. For instance, Cao et al. (Fan et al., 2023) conducted a numerical study on the disastrous mechanism of seepage instability considering the variable mass effect, demonstrating the potential of simulation techniques in handling complex flow boundary problems. Combining non-linear flow equations with digital rock simulation, Fan et al. (Nabipour et al., 2024) and Nabipour et al. (Berg et al., 2024) proposed boundary layer effect correction models, which can more accurately predict flow resistance in micro-scale pore throats. The integrated unsteady-state core flooding method developed by Berg et al. (Li et al., 2023) allows for the simultaneous acquisition of relative permeability and capillary pressure curves, realizing multi-parameter integrated classification. By integrating parameters such as fractal dimension, TEM-Function, threshold pressure difference, and relative permeability curves, a multi-dimensional classification model can be constructed. This model accurately characterizes reservoir quality and flow potential, providing solid support for the classification evaluation and optimized development design of high-quality low-permeability reservoirs. However, most existing studies either focus on pore structure characterization or flow behavior independently, and few attempts have been made to quantitatively integrate pore-throat topology with non-linear flow response into a unified reservoir classification framework.

Although the aforementioned studies have made significant progress in their respective fields, research on the quantitative mapping relationship between the microscopic structure and macroscopic seepage capacity of specific complex lithologies remains relatively scattered. Existing reservoir evaluations often focus on single-dimensional parameters and lack a classification system that systematically integrates microscopic topological structures with macroscopic non-linear flow characteristics. In view of this, this study comprehensively employs various methods, including rate-controlled mercury injection (RCMI), nuclear magnetic resonance (NMR), non-Darcy flow experiments, and digital rock simulation, taking the W1 and W2 blocks as examples. By systematically integrating the differences in reservoir pore-throat configurations and flow capacities, this study establishes a logical framework from microstructure characterization, to macroscopic non-linear seepage response, and finally to multi-parameter reservoir classification.

2 Experimental samples

The core samples selected for this study were obtained from the low-permeability reservoirs of the Paleogene Liushagang Formation in the Weixinan Sag, Beibu Gulf Basin, northern South China Sea. Based on differences in geological characteristics, the study targets are divided into two blocks, W1 and W2; specific sampling parameters for the cores are listed in Table 1.

The coring depth of the W1 block ranges from 3,159.7 to 3,308.8 m. This horizon belongs to the proximal braided river delta front sub-facies, where reservoir sand bodies are primarily

TABLE 1 Information on tested samples.

Block	Sample ID	Depth/m	Lithology	Porosity/%	Permeability/mD	Block	Sample ID	Depth	Lithology	Porosity/%	Permeability/mD
W2	W2-1	3,176.66	Gravelly coarse sandstone	11.8	1.64	W1	W1-19	3,225.98	Gravelly medium coarse sandstone	16.7	1.56
	W2-2	3,176.76		11.6	1.7		W1-20	3,225.98		17.6	1.13
	W2-4	3,178.3	Medium-coarse sandstone	14.8	2.88		W1-21	3,225.98		16.2	1.75
	W2-5	3,178.3		14.6	2.37		W1-22	3,250.34	16.1	5.7	
	W2-6	3,178.3	Fine sandstone	14.4	2.78		W1-23	3,304.65	11.5	4.59	
	W2-7	3,181.32		11.8	0.1523		W1-24	3,304.65	12.8	4.4	
	W2-8	3,181.32		12	0.1787		W1-25	3,306.2	10.8	0.2675	
	W2-10	3,186.1	Gravel sandstone	10.8	0.5779		W1-26	3,306.5	15.3	0.5311	
	W2-11	3,186.1		11.4	0.9835		W1-28	3,159.7	4.3	1.21	
	W2-12	3,186.1	Gravelly fine sand	12.7	0.8568		W1-29	3,159.7	4.1	0.4332	
	W2-13	3,189.04		11.8	0.8654		W1-30	3,159.7	4	0.4986	
	W2-14	3,189.04		12.3	0.1673		W1-31	3,303.41	6.5	0.0183	
	W2-15	3,189.04	Medium-coarse sandstone	12.1	0.2519		W1-32	3,308.81	3.8	0.0136	
	W2-16	3,183.15		13.4	1.59		W1-34	3,305.2	12.1	0.0728	
	W2-17	3,183.15		13.7	2.59		W1-35	3,305.2	12.8	0.0762	
							3,307.54	Gravelly sandstone	13.9	16.4	

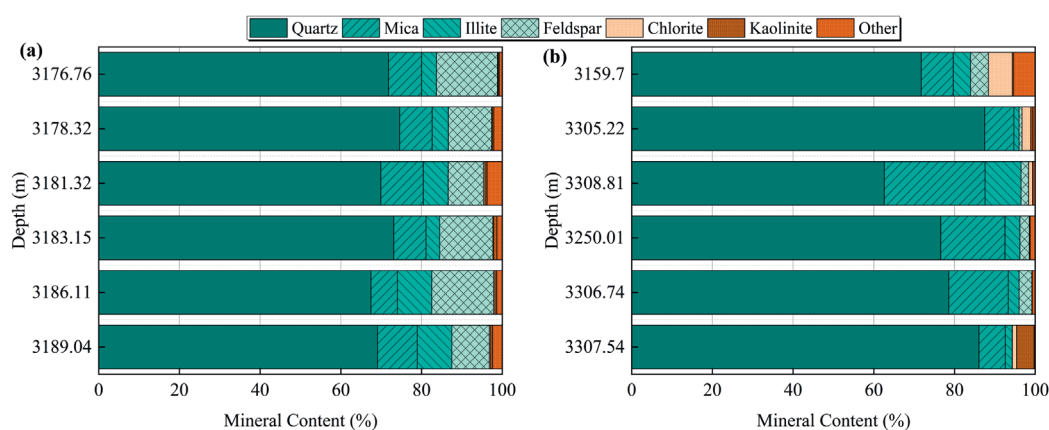


FIGURE 1 Comparison of core mineral composition between the W2 (left) and W1 (right) blocks. (a) W2-I1. (b) W1-I3.

developed in underwater distributary channel and mouth bar micro-facies. It is characterized by proximity to the provenance, rapid sedimentation rate, and lateral connectivity segmented by faults. The lithofacies of block W2 are mainly medium-coarse sandstone, while that of block W1 is mainly gravelly sandstone and gravelly medium-coarse sandstone. The gas-measured porosity of the lithology in the W1 block ranges from 3.8% to 17.6%, with an average of 11.73%, while the permeability ranges from 0.01 to 14 mD, with an average of 2.26 mD. As shown in Figure 1b, whole-rock mineral analysis indicates that this block is dominated by quartz and is classified as feldspathic quartz sandstone or lithic quartz sandstone, with a relatively high content of mica in the interstitial material (Figure 1).

The coring depth of the W2 block is concentrated between 3,176.7 and 3,189.0 m. This horizon mainly develops a sub-lacustrine fan depositional system, originating from gravity flows within a deep to semi-deep lake background. The samples were mainly collected from the braided channel micro-facies of the middle fan sub-facies. The gas-measured porosity of the lithology in the W2 block ranges from 10.1% to 14.8%, with an average of 12.52%, and the permeability is distributed between 0.1 and 2.9 mD, with an average of 1.31 mD. As shown in Figure 1a, in terms of mineral composition, this block is dominated by quartz and feldspar and belongs to feldspathic quartz sandstone, with clay minerals mainly composed of illite and mica.

3 Test methods

To characterize the pore-throat structure and flow behavior of the studied reservoirs, a series of laboratory experiments and digital core simulations were conducted.

Rock pore structure was first quantified using constant-rate mercury injection (RCMI) and nuclear magnetic resonance (NMR) measurements. The RCMI tests were performed with a Coretest ASPE-730 apparatus, with mercury injection pressures ranging from 0 to 1,000 psi and a constant injection rate of 0.00005 mL/min, ensuring quasi-static intrusion conditions. NMR measurements were conducted using a MicroMR12-110H-1 analyzer with a

resonance frequency of 11.793 MHz, magnetic field strength of 0.3 ± 0.03 T, and a coil diameter of 25 mm. Prior to NMR testing, samples were centrifuged to the bound-water state using a YC-1C high-speed centrifuge (maximum speed of 10,000 rpm; maximum displacement pressure of 2.07 MPa). Based on T_2 relaxation spectra inversion, key parameters including porosity, T_2 cutoff values, and mobile fluid saturation were obtained.

Oil-water two-phase flow behavior was evaluated through unsteady-state relative permeability experiments conducted in accordance with the SY/T 5345-2007 standard. The experiments were carried out under a constant pressure difference of 8 MPa. The starting pressure gradient (TPG) was determined using a step-wise flow rate method, with flow rates sequentially set to 0.005, 0.01, 0.02, 0.05, and 0.10 mL/min. Each flow step was maintained for no less than 3 h to ensure stable pressure equilibration before data acquisition.

Three-dimensional digital core reconstruction and pore-scale flow simulations were performed using a MicroXCT-200 micro-CT scanner. The scanning resolution for whole-core samples was 13 μm , while sub-samples were scanned at higher resolutions ranging from 0.5 to 3 μm . The acquired grayscale images were processed through filtering, segmentation, and geometric topology analysis. Pore structures were segmented using the watershed algorithm, and pore network models were extracted using the maximum ball algorithm. Based on the reconstructed pore network, oil-water displacement processes were simulated, and relative permeability curves were calculated using the lattice Boltzmann method (LBM), enabling three-dimensional visualization of pore space distribution and fluid displacement behavior.

Prior to all experiments, core samples were thoroughly cleaned using Soxhlet extraction (toluene for 48 h to remove residual hydrocarbons, followed by ethanol for 36 h to remove salts) and dried at 80 $^{\circ}\text{C}$ to constant weight to minimize clay mineral alteration. Simulated formation fluids were employed throughout the experiments: the oil phase consisted of a mixture of kerosene and degassed crude oil with a viscosity of 4.5 mPa·s at 50 $^{\circ}\text{C}$, while the water phase was synthetic brine with a salinity of 35,000 mg/L. These experimental conditions ensured consistency and comparability among different measurements.

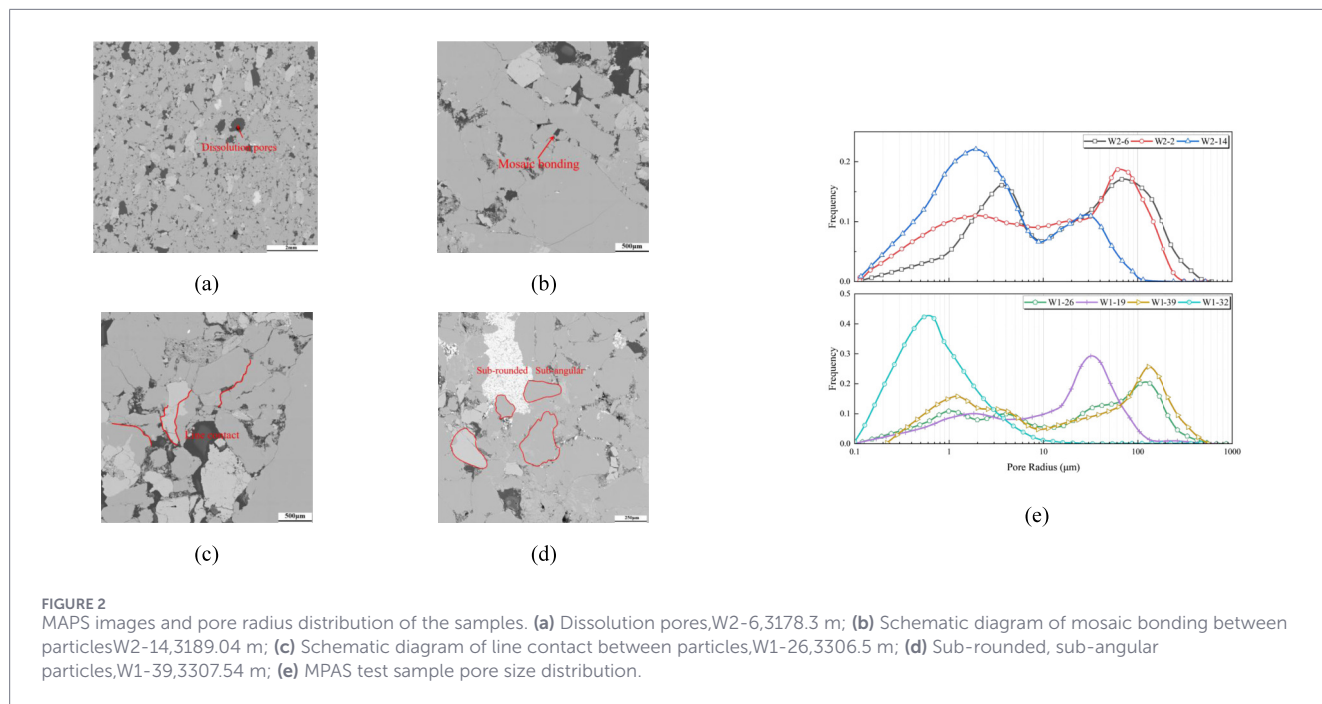


TABLE 2 Summary of MAPS test results.

Block	Sample ID	Grain sorting	Pore radius/ μm	Pore-radius peak/ μm
W2	W2-2	Very poorly sorted	50–200	60
	W2-6	Poorly sorted	0.5–200	No distinct peak
	W2-14	Moderately sorted	0.1–100	1–4
W1	W1-19	Poorly sorted	30–500	1; 130
	W1-26	Very poorly sorted	50–500	35
	W1-32	Well sorted	0.1–4	0.6
	W1-39	Poorly sorted	0.2–400	1; 150

4 Analysis of test results

4.1 Micro-pore throat types

A thorough analysis of 7 large-area scanning electron microscope images of sandstone samples from the W1-I3 and W2-I1 reservoirs in the designated study area has been conducted, indicating that the particles in both reservoirs exhibit line contact, with a compressive cementation mechanism (Figures 2a–d). The predominant pore types that have been observed are dissolution pores and intergranular fractures. The pores demonstrate a relative regularity in shape, exhibiting rectangular and polygonal forms, with pore diameters primarily ranging from 50 to 200 μm , and some larger pores reaching 200–500 μm . The fracture morphology is diverse, primarily including plate-like, necked, and punctate forms, with fracture radii varying from tens of micrometers to hundreds of micrometers (Figure 1e; Table 2).

4.2 Analysis of micro-pore throat structure characteristics

This study integrates mercury injection and nuclear magnetic resonance (NMR) techniques to conduct a synergistic analysis and systematic quantitative characterization of the microscopic pore–throat geometry and pore size distribution characteristics of the reservoirs in the target area.

4.2.1 Constant-rate mercury porosimetry test

The mercury saturation levels of the W1-I3 reservoir, as determined by testing 11 samples from two reservoirs in the study area, range from 30% to 53%. The analysis revealed that the pores in the reservoir primarily consist of small throats, with pore radii measuring between 137 μm and 150 μm , and throat radii ranging from 0.4 μm to 5 μm . The throat-to-pore ratio of the reservoir ranges

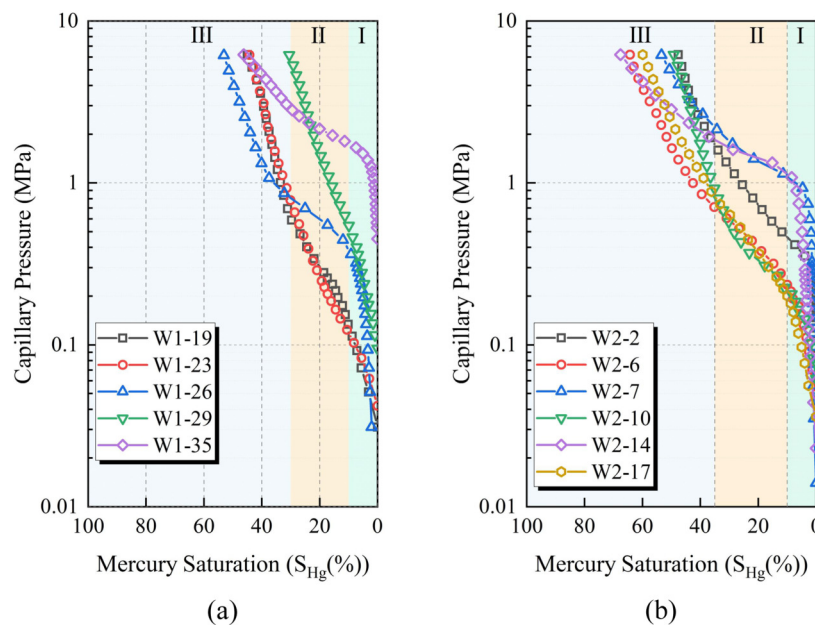


FIGURE 3 Mercury injection capillary pressure (MICP) curves for the study area. (a) W1-I3. (b) W2-I1.

from 50 to 400, indicating variations in the size distribution of the pores. The mercury saturation of the W2-II reservoir ranged from 47% to 70%, primarily consisting of small pore throats. The porosity and pore radius were found to range between 140 μm and 150 μm , with throat radii varying from 0.5 μm to 2 μm and a pore throat ratio of 95–300.

As illustrated in Figure 3, the mercury penetration curve for low-permeability reservoirs can be divided into three distinct stages: In the initial phase (Stage I), mercury rapidly fills large pore throats at low pressure, resulting in a steep curve. The characteristics of the throat have minimal influence on mercury penetration. In the subsequent phase (Stage II), as pressure increases, mercury enters finer, poorly connected pores. This causes the curve slope to decrease. In the final phase (Stage III), at high pressure, mercury enters isolated micro-pores or nanoscale throats. This causes the curve to rise again.

4.2.2 Nuclear magnetic resonance testing

The study revealed that, under saturated water-bearing conditions, the NMR T_2 spectra of the target reservoir samples exhibited a typical double-peak characteristic. It has been demonstrated that nuclear magnetic resonance (NMR) experiments conducted on dense sandstone in a saturated water-bearing state have the capacity to reveal the overall distribution of pores in rock samples (Yue et al., 2022). An analysis of the experimental curves reveals that the majority of samples contain pores of varying sizes. However, the composition of the W1 samples is primarily micro-pores, while the W2 samples are predominantly constituted of medium-sized and large pores (Figure 4). In the W1-21 and W1-24 samples, the left T_2 peak is significantly higher than the right peak, indicating that micro-pores dominate in these samples; whereas in the W2-5 sample, the intensities of the left and right

peaks are similar, suggesting that the volume fractions of medium-sized and large pores are roughly equivalent. For the W2-12, W2-15, and W1-30 samples, although the right-side peak has increased, it remains lower than the left-side peak, and the two peaks are connected smoothly without any obvious breaks. This indicates that the proportion of larger pores gradually increases in these samples, but micro-pores still dominate.

Combining NMR and RCMI test results, under identical conditions, the average pore radius determined by the mercury porosimetry method and the logarithmic mean of the transverse relaxation time T_2 are selected. The surface relaxation rate is calculated using the following Equations 1–3 (Guo et al., 2014):

$$T_{2LM} = \exp\left(\frac{\sum \ln T_{2i} \times \varphi_i}{\sum \varphi_i}\right) \quad (1)$$

$$\gamma_p = \frac{\sum (r_{j-1} + r_j)(S_j - S_{j-1})}{2 \sum (S_j - S_{j-1})} \quad (2)$$

$$\rho = \frac{\gamma_p}{T_{2LM} \times F_s} \quad (3)$$

In the equation, T_{2i} denotes the T_2 value (ms) at point i ; φ_i represents the corresponding NMR signal amplitude (a.u.); r_j indicates the throat radius (μm) for the j pressure step; S_j signifies the mercury saturation (%) at step j ; shape factor $F_s = 1, 2, 3$, with 2 selected in this study.

The T_2 spectrum subsequent to centrifugation indicates that bound water is predominantly distributed in the small and medium pores of the rock core. In comparison with the T_2 spectrum under saturated water-bearing conditions, alterations in the spectral morphology of the same sample following centrifugation have been shown to reflect the distribution characteristics of mobile fluids. For instance, samples W1-24 and W1-30, as well as W2-12 and W2-15, exhibited virtually

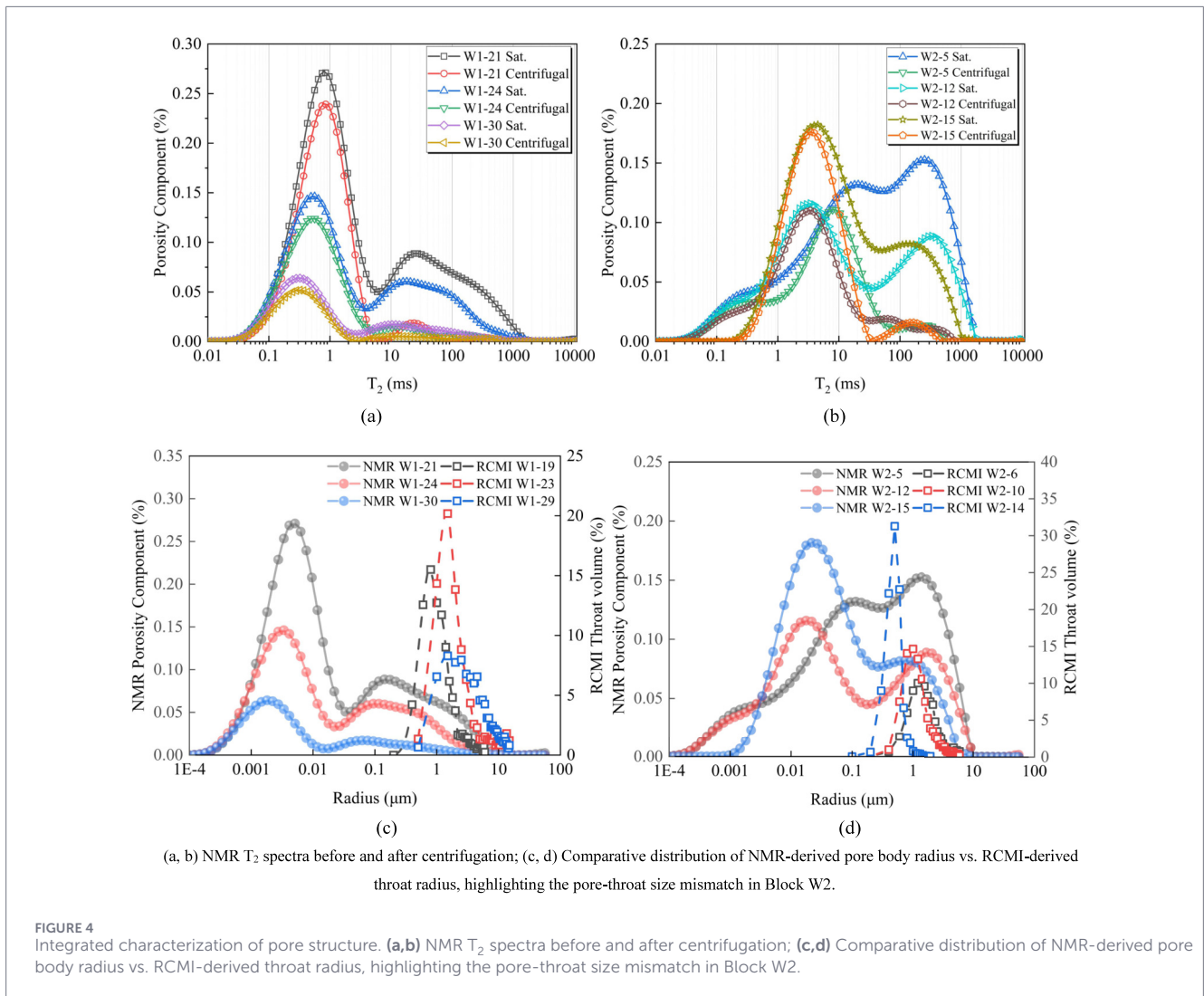


FIGURE 4 Integrated characterization of pore structure. (a,b) NMR T_2 spectra before and after centrifugation; (c,d) Comparative distribution of NMR-derived pore body radius vs. RCMI-derived throat radius, highlighting the pore-throat size mismatch in Block W2.

unchanged morphology and peak values for the left-hand peak. This finding suggests that these samples contain negligible amounts of mobile fluid within their micro-pores. Furthermore, it was observed that for the majority of samples, the intensity of the right-hand peak underwent a substantial decrease following the process of centrifugation. This finding suggests that a certain quantity of mobile fluid persists within the larger pores. The variability in the extent of right-side peak decay among different samples is indicative of the heterogeneity in their mobile fluid content. For instance, the right-side peak decay in the W2-5 sample is more pronounced, while the right-side peak decay in the W1-21 sample is relatively minor, indicating that the former contains significantly more mobile fluid in its medium-to-large pores than the latter.

Based on the corrected ρ values (Table 3), the NMR T_2 spectrum was converted into a pore size distribution and compared with the RCMI throat radius distribution (Figures 4C,D). A mismatch between pore and throat sizes was observed, particularly in the W2 block. As shown in Figure 4D, while the NMR-derived pore volume distribution exhibits a dominant peak in the 1–10 μm range, confirming the presence of substantial reservoir space (dissolved pores), RCMI data indicate that connected throats are strictly confined to <1 μm . This quantitative evidence

TABLE 3 Summary of surface relaxation for each sample.

Sample ID	$\gamma_p/\mu\text{m}$	T_{2LM}/ms	$\rho/\mu\text{m}\cdot\text{s}^{-1}$
W1-19	143.997	16.547	4.351
W1-23	137.350	13.608	5.046
W1-29	142.412	11.021	6.460
W2-6	147.076	22.428	3.278
W2-10	140.882	12.669	5.560
W2-14	142.077	11.631	6.107

corroborates the wide-pore-narrow-throat topology proposed in the Mechanism section.

The analysis of the mobile fluid parameters of samples from the W block's dense sandstone reservoir reveals significant differences, thus indicating strong heterogeneous characteristics in the reservoir's internal fluid mobility. The T_2 cutoff value ($T_{2cutoff}$, abbreviated as T_{2c}) is the key parameter for defining bound fluid and mobile fluid. The T_2 cutoff value is typically determined using

TABLE 4 Summary of NMR movable fluid analysis in block W.

Sample ID	NMR porosity/%	Permeability/mD	$T_{2\text{ Cutoff}}$ /ms	NMR water sat./%	Movable fluid sat./%
W1-21	14.30	1.75	2.00	56.70	43.30
W1-24	8.50	4.40	2.60	60.80	39.20
W1-30	3.10	0.50	1.00	65.80	34.20
W2-5	13.30	2.37	19.30	41.50	58.50
W2-12	9.40	0.86	15.70	57.20	42.80
W2-15	11.30	0.25	12.75	59.10	40.90

the centrifugal calibration method. The specific procedure of this method is as follows: a horizontal line is drawn at the peak of the T_2 spectrum accumulation curve under centrifugal conditions. The horizontal line intersects with the T_2 spectrum accumulation curve under saturated conditions. A perpendicular line is drawn from the intersection point to the horizontal axis, and the T_2 relaxation time corresponding to the foot of the perpendicular line is the T_{2c} value (Wu et al., 2021). The calculation results indicate that the T_{2c} values of the study samples are distributed within the range of 1–20 ms, with an average value of approximately 8.89 ms (Table 4).

The determination of the mobile fluid percentage (MFP) in rock samples is primarily achieved through two methods: the cutoff method and the centrifugal method (Jia et al., 2024). The principle of the cutoff method is to set a T_{2c} threshold: fluids with relaxation times greater than T_{2c} are considered mobile fluids, while those with relaxation times less than T_{2c} are considered bound fluids; the MFP is the ratio of the volume of mobile fluids to the total volume of saturated fluids. The method is predicated on a two-peak pore model that is idealised, assuming that fluid in large pores is completely mobile, while fluid in small pores is completely confined. The centrifugal method is a simulation of the displacement process during core centrifugation, whereby MFP is defined as the ratio of the volume of fluid displaced by centrifugation (i.e., the difference in fluid volume before and after centrifugation) to the original saturated fluid volume. When combined with the characteristic analysis of T_2 spectra before and after centrifugation of samples from the target block (large pores contain partially bound fluid, while small pores contain a small amount of mobile fluid), the centrifugal method more accurately reflects the actual mobile fluid content in the reservoir compared to the cutoff method (Zhao et al., 2020). The calculation of MFP using the centrifugal method is achieved through the following steps: firstly, the difference between the maximum values of the cumulative T_2 spectra at the saturated state and the centrifugal state must be calculated; secondly, the ratio of this difference to the maximum value of the cumulative spectrum at the saturated state is the MFP. The MFP of sandstone samples ranges from 34.2% to 58.5%, with an average value of 43.15%, as calculated.

4.3 Macroscopic non-linear flow characteristics

The microscopic pore-throat characteristics and fluid mobility distributions analyzed in Sections 3.1 and 3.2 provide the physical

basis for reservoir seepage capacity. However, to accurately evaluate the development potential of low-permeability reservoirs, it is essential to quantify their macroscopic flow behaviors under dynamic conditions. Consequently, this section investigates the non-linear flow characteristics of the study area, focusing specifically on the TPG and oil-water relative permeability. These macroscopic flow parameters serve as direct manifestations of the microscopic topological constraints previously discussed.

4.3.1 Initial pressure gradient test

In the context of fluid flow through a low-permeability reservoir, the existence of an additional pressure gradient is imperative in order to overcome the resistance posed by the rock surface adsorption film or hydration film, thus enabling the fluid to flow. This additional pressure gradient is referred to as the TPG (TPG) (Zhang et al., 2017). In low-permeability sandstone reservoirs, the flow pattern is typically characterized by low-velocity non-Darcy behavior due to the complex pore-throat structure. Accordingly, the TPG obtained from nonlinear flow experiments was employed to analyze the reservoir flow mechanisms of the 12 samples from the study area.

As shown in Table 5, the nonlinear flow test results indicate that significant differences exist in TPG values both within and between reservoirs. Specifically, the TPG values of the W2-I1 and W1-I3 reservoirs range from 0.20 to 8.10 MPa/m and 0.02–16.70 MPa/m, respectively, with average values of 2.65 MPa/m and 6.80 MPa/m, the higher average TPG observed in Block W1 is mainly attributed to strong intra-block heterogeneity. According to the results of MAPS analysis, the W1-I3 reservoir is mainly composed of intergranular pores and dissolution pores, which are characterized by relatively larger throat radii and better connectivity of flow pathways. In contrast, the W2-I1 reservoir is dominated by micropores and fine intergranular pores, featuring smaller throat radii and poorer pore sorting. This pore structure results in higher flow path tortuosity and facilitates the formation of micro-bypasses during water flooding (Table 5).

In previous studies (Zhang et al., 2021), the pressure gradient (λ) and permeability (k) in low-permeability reservoirs satisfy a power function relationship (Equation 4):

$$\lambda = a \cdot k^b \quad (4)$$

In the equation, the symbol a represents the basic flow resistance, which is influenced by both the pore structure and the fluid properties. The symbol b is a negative exponential term reflecting the sensitivity of permeability to pressure gradients, with a larger

TABLE 5 Results of the TPG test.

Sample ID	Porosity/%	Permeability/ mD	TPG/MPa/m
W1-20	17.60	1.13	2.44
W1-22	16.10	5.70	0.02
W1-25	10.80	0.28	6.82
W1-28	4.30	1.21	1.84
W1-31	6.50	0.02	16.63
W1-34	12.10	0.08	13.02
W2-1	11.80	1.64	0.27
W2-4	14.80	2.88	0.15
W2-8	12.00	0.18	8.09
W2-11	11.40	0.98	3.31
W2-13	11.80	0.87	3.52
W2-16	13.40	1.59	0.55

absolute value indicating a faster increase in pressure gradients under low permeability conditions.

To further analyze the relationship between macroscopic physical properties and flow resistance, a regression analysis between permeability and TPG was conducted. As illustrated in Figure 5, a clear power-law relationship exists between permeability and TPG for both blocks. Although the permeability ranges of the W1 and W2 blocks are comparable, the fitted power-law exponent for Block W2 is significantly larger than that for Block W1. This indicates that the flow resistance in the W2 reservoir increases more rapidly with decreasing permeability, reflecting stronger hydraulic sensitivity to physical property deterioration. This behavior is closely related to the combined effects of finer pore-throat structures and enhanced boundary-layer resistance induced by clay mineral hydration in the W2 reservoir.

4.3.2 Analysis of oil-water phase permeability characteristics

Based on the experimental results of oil-water relative permeability tested via the unsteady-state method, the seepage curves of reservoirs in the study area exhibit two distinctly different characteristics, which are defined in this paper as the “Inefficient Flow Regime” and the “Efficient Flow Regime” (Figure 6). The “Inefficient Flow Regime” is characterized by a narrow two-phase co-flow region and a sharp decline in oil relative permeability with increasing water saturation; this regime typically corresponds to low oil displacement efficiency. Conversely, the “Efficient Flow Regime” exhibits a wider two-phase co-flow region and demonstrates high-efficiency seepage characteristics during both the water-free oil production period and the final displacement stage.

In the context of low-permeability reservoirs, the range of water saturation levels is reported to be from 31% to 33%. As water saturation increases, the relative permeability of the oil phase decreases linearly, while the increase in the relative permeability

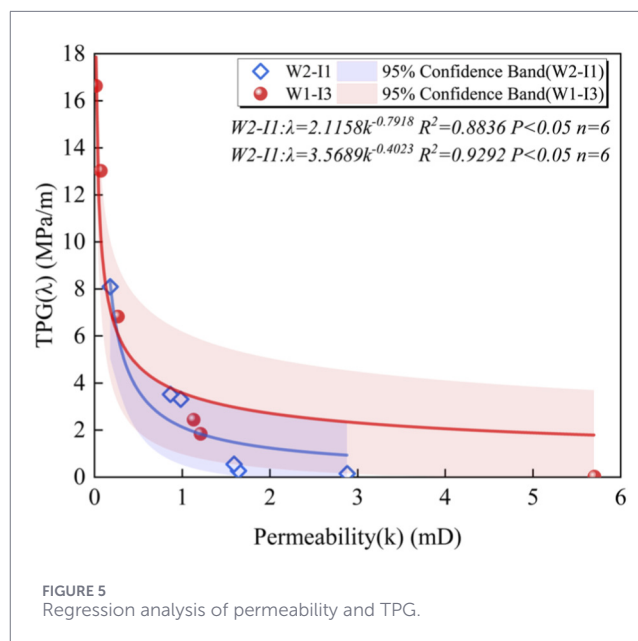


FIGURE 5 Regression analysis of permeability and TPG.

of the water phase is relatively slow. During the water-free period, the oil recovery efficiency of such reservoirs is only 10%–15%. Furthermore, the saturation range for simultaneous oil and water phase penetration is typically below 20%, resulting in a low waterflooding efficiency of approximately 33%–38%. The water saturation at the intersection point is marginally below 50%, with the corresponding relative permeability generally less than 0.10. Such reservoirs exhibit pronounced hydrophilic or hydrophilic properties. In the context of hydrophilic reservoirs, during the process of water-driven oil recovery, the water phase has been observed to advance along the pore walls, thereby driving the oil phase. As the water saturation level rises, the thickness of the water film on the surface of the particle pore throats increases [24]. Concurrently, as the radius of the pore throat decreases, the ratio of the water film thickness to the radius of the pore throat increases. This, in turn, results in a greater impact of the water film thickness on the flow velocity of the oil phase. Consequently, such reservoirs exhibit higher residual oil saturation and lower ultimate water-driven oil recovery efficiency.

In the context of high-efficiency flow reservoirs, the bound water saturation level exhibits fluctuations within the range of 27%–32%. The relative permeability of the oil phase decreases slowly with increasing water saturation, and the range of co-flow between the oil and water phases can reach approximately 50%, resulting in a final waterflooding efficiency as high as 60%. The water saturation at the intersection point ranges from 52% to 73%, corresponding to a relative permeability of 0.10–0.15 mD. Such reservoirs characteristically manifest water-saturated or marginally water-saturated properties. The inhibitory effect of residual water in the pores on oil phase flow is significantly reduced due to pore throat diameters >1.00 μm and low immobile water saturation.

In summary, the anatomical structure of the throat has a significant impact on phase permeability behavior. As demonstrated in Figure 5, there is a positive correlation between the average throat radius and the co-permeability zone between the oil and water phases, as well as the water saturation corresponding

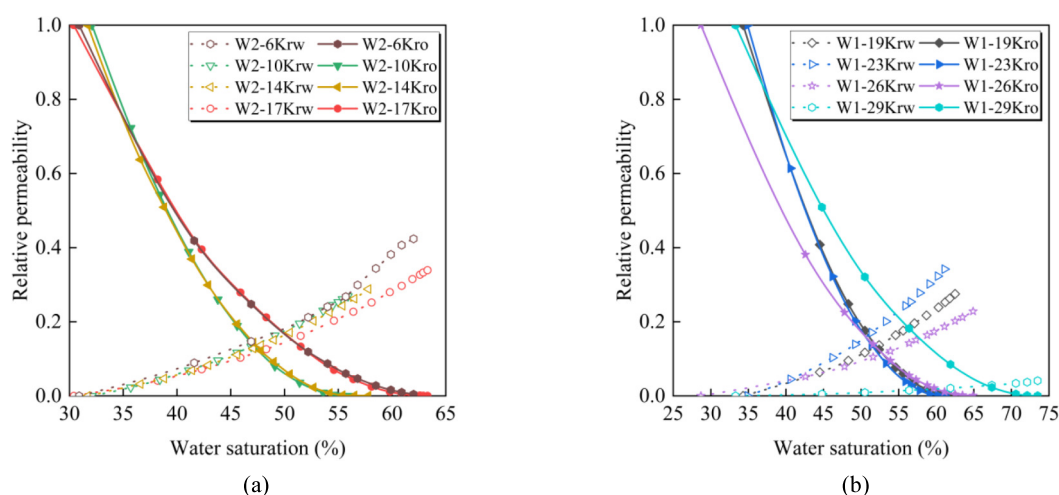


FIGURE 6
Experimental results of oil–water relative permeability. (a) Inefficient flow regime. (b) Efficient flow regime.

to residual oil. As the throat radius increases, the co-permeability zone expands synchronously. This phenomenon is attributed to the relatively high relative permeability of the water phase, which significantly affects waterflooding recovery efficiency.

4.4 Flow mechanism analysis and digital core simulation

The macroscopic flow experiments presented in Section 3.3 revealed the distinct non-linear seepage characteristics of the reservoir. To investigate the microscopic nature of these flows, specifically the fluid distribution within pore networks, this section employs digital core simulation technology to simulate the oil-water migration behavior during the displacement process. Focusing on the simulation verification of oil-water relative permeability, the results are validated against physical experimental data. By integrating these findings with the aforementioned experimental analysis, the intrinsic control mechanisms of pore-throat topology on the reservoir's flow capacity are ultimately elucidated.

4.4.1 Digital core simulation

To further investigate pore structure characteristics and pore–throat fluid flow mechanisms, four representative core samples were selected for micro-CT scanning. Considering the limited field of view inherent to high-resolution micro-CT imaging, the samples were deliberately chosen to represent the dominant lithofacies of the study area. Specifically, samples from Block W1 were selected from the gravelly coarse sandstone facies, which constitutes the primary reservoir lithology in this block, while samples from Block W2 were taken from the clay-rich medium sandstone facies that dominates reservoir development in that block. By focusing on the main reservoir lithofacies in each block, the constructed digital cores are expected to capture the characteristic pore–throat architecture and flow pathways of the principal reservoir bodies, thereby ensuring geological and hydraulic representativeness at the facies scale.

For the digital core reconstruction, a sub-volume of $1,200 \times 1,200 \times 1,200$ voxels was extracted from the raw data and processed through filtering and binarization. This analysis volume significantly exceeds the Representative Elementary Volume (REV) required for medium-to-fine-grained sandstones, minimizing the uncertainty associated with the resolution-field-of-view tradeoff and ensuring that the calculated topological parameters (e.g., coordination number) are intrinsic to the rock matrix.

In the Lattice Boltzmann Method (LBM) simulations, the fluid properties were set to match the experimental conditions, maintaining the same oil-water viscosity ratio. Periodic boundary conditions were applied in the flow direction to mimic an infinite porous medium, while the half-way bounce-back scheme was adopted at solid-fluid interfaces to enforce no-slip conditions. To reflect the wetting characteristics observed in experiments, the contact angle was set to 30° .

Through these simulations, parameters such as porosity, permeability, pore radius, throat radius, coordination number, shape factor, connectivity, and two-phase flow behavior were calculated (Table 6). In terms of permeability, the LBM simulation results were validated against physical experimental data. Taking representative samples as examples, the simulated permeability of sample W2-6 was close to the experimental value (2.78 mD), with a relative error of only 4.3%; the relative deviation for sample W1-23 compared to the experimental value (4.59 mD) was also controlled within 17%. Although the simulation deviation slightly increased for some low-permeability tight samples due to strong heterogeneity, the overall simulation results remained consistent with the experimental results in terms of order of magnitude, indicating that the constructed pore network model can effectively reflect the true flow channel characteristics of the reservoir.

Secondly, regarding multiphase flow characteristics, the simulated oil–water relative permeability curves exhibited consistency with the experimental curves in terms of saturation endpoints and morphological features (Figure 7). The simulation results accurately reproduced the differentiated fluid distribution

patterns of the W1 and W2 blocks: the simulated irreducible water saturation of sample W1-19 was 33.5%, consistent with the experimental average of the W1 block (27%–32%), and the curve presented a characteristic wide two-phase co-flow region. In contrast, the simulation results for sample W2-6 reproduced the characteristics of inefficient flow, with its simulated residual oil saturation (32.13%) aligning with the phenomenon of high residual oil observed in experiments.

4.4.2 Mechanism of pore structure control on flow

The integrated analysis of microscopic experiments reveals that the macroscopic flow capacity is fundamentally constrained by the pore-throat topological structure. While the pore radii across all samples are relatively uniform, the permeability varies by orders of magnitude. This fundamental contradiction indicates that the reservoir flow capacity is not controlled by the storage space, but is strictly constrained by the connectivity and radius of the transport channels. The characteristic ‘wide pore, narrow throat’ configuration creates a severe bottleneck effect. As evidenced by the mercury intrusion curves (Section 3.2.1), high-permeability samples exhibit a steep Stage I ascent, corresponding to the rapid filling of macropores through well-connected throats. Conversely, the prolonged plateau-like characteristic (Stage II) in low-permeability samples signifies a complex network dominated by narrow throats and micro-fractures. Physically, this plateau represents the high resistance required to overcome the Jamin effect within these restricted paths, a conclusion further supported by the high tortuosity values listed in Table 7. Consequently, although the total porosity remains high, the effective flow channels are severely constricted, preventing the effective mobilization of fluids stored in large pores.

Beyond geometric constraints, the mineral composition exerts a critical physico-chemical control on the flow boundary layer, which constitutes the intrinsic mechanism for the high TPG observed in Block W2. Specifically, regarding wettability control, the W2 block is characterized by a high content of clay minerals, such as illite and mica. In contrast to the quartz-dominated rigid framework of the W1 block, these clay minerals possess a significantly higher specific surface area and surface energy. This physico-chemical property enhances the adsorption capabilities at the solid–liquid interface, facilitating the formation of thick adsorbed water and hydration films on the pore–throat surfaces. Consequently, the effective flow radius of the fluid is compressed. When this boundary layer effect is superimposed on the fine throat radii of the W2 block, the Jamin effect is significantly amplified. Therefore, the high flow resistance in the W2 block is the result of the synergistic effect of high clay content and fine throats.

In summary, the reservoir quality in the study area is controlled by the coupling of microscopic pore-throat topology and mineral composition. The “wide-pore, narrow-throat” configuration combined with high clay content induces significant boundary layer effects, leading to the observed high TPGs and inefficient flow regimes. These multi-scale geological factors determine that conventional porosity and permeability parameters are insufficient for accurately defining effective reservoirs. Consequently, a comprehensive multi-parameter evaluation system is required. The following Section 4 will establish a quantitative classification

standard based on these flow mechanisms to guide the efficient development of these low-permeability reservoirs.

5 Reservoir classification based on macro-physical properties and microstructure

5.1 Reservoir classification standards

Given the strong heterogeneity and complex seepage mechanisms of low-permeability reservoirs, single-scale characterization methods are often constrained by inherent limitations. To ensure the rigor of the evaluation, it is crucial to explicitly acknowledge the uncertainties associated with each technique. Firstly, regarding rate-controlled mercury injection, the interpretation relies on a bundle of cylindrical capillaries model, which simplifies the complex topology of actual pore networks. The shielding effect of narrow throats may lead to an underestimation of pore body sizes, particularly in samples with high aspect ratios like those in the W2 block. Secondly, for NMR analysis, the transformation from T_2 relaxation time to pore size distribution depends heavily on surface relaxivity. In this study, a constant was applied; however, local variations in mineralogy could introduce uncertainty into the pore-size calculation. Thirdly, Digital Rock Simulation is constrained by the trade-off between resolution and field of view. Although the scanning resolution reached 1 μm micropores below this threshold, and the segmentation process may introduce minor personal dependent bias affecting coordination number calculations.

To overcome these method-specific constraints and define the reservoir mobilization boundary accurately, this study adopts a strategy of multi-method complementarity and multi-scale calibration. We mitigated individual limitations by cross-validating the capillary pressure curves from RCMI with LBM simulations, although the potential influence of sub-resolution connectivity remains a source of uncertainty. On this basis, by systematically integrating the throat characterization from RCMI, the full pore-size coverage from NMR, and the topological analysis from digital rock physics, the systematic errors associated with single methods are effectively minimized. Following the principle of prioritizing seepage capacity while considering storage space, multi-source experimental data were synthesized to construct a reliable multi-parameter coupled comprehensive reservoir classification evaluation system, achieving a precise characterization of the reservoir’s seepage capacity and development potential.

Although permeability represents the macroscopic manifestation of interactions between microscopic pore structures and fluids, it is widely recognized as a representative indicator for reservoir evaluation in engineering practice. Therefore, this study establishes a permeability classification framework integrating statistical regression with engineering constraints for reservoir categorization. Based on the actual data distribution in the study area and low-permeability reservoir classification criteria, three key permeability cutoff values were further refined: 0.5 mD for the effective flow limit, 2.0 mD for the nonlinearity transition point, and 10.0 mD for approximate Darcy flow. Second, thresholds for other parameters (TPG, average throat radius, and MFS) were

TABLE 6 Digital core pore network models and flow simulation results for samples from block W.

Sample ID	Porosity/%	Permeability/ mD	Connate water sat./%	Residual oil sat./%	Final oil recovery/%	Mean pore radius/ μm	Mean throat radius/ μm	Connectivity/%	Coordination number
W2-6	13.3	2.66	29.9	32.13	54.2	55.5	4.7	59.0	5.8
W2-17	11.5	2.255	30.2	35.1	49.7	56.0	5.1	85.2	3.6
W1-19	16.5	1.21	33.5	35.9	46.0	79.9	6.4	83.8	3.4
W1-23	9.5	5.37	33.2	38	43.1	21.5	4.5	74.4	2.9

determined by mapping these permeability cutoff values onto their respective cross-plots. Regarding the influence of multiple parameters on classification, based on their degree of control over fluid migration and the characteristics of the target area, this study identifies TPG and average throat radius as primary controlling parameters, while MFS and porosity serve as secondary auxiliary parameters. It should be noted that the classification system adopts a “Macroscopic Definition, Microscopic Verification” principle. The microscopic topological parameters derived from digital rock physics (e.g., Coordination Number) serve as auxiliary descriptive indicators to visualize the underlying pore-structure mechanisms of each type, rather than functioning as rigid statistical thresholds.

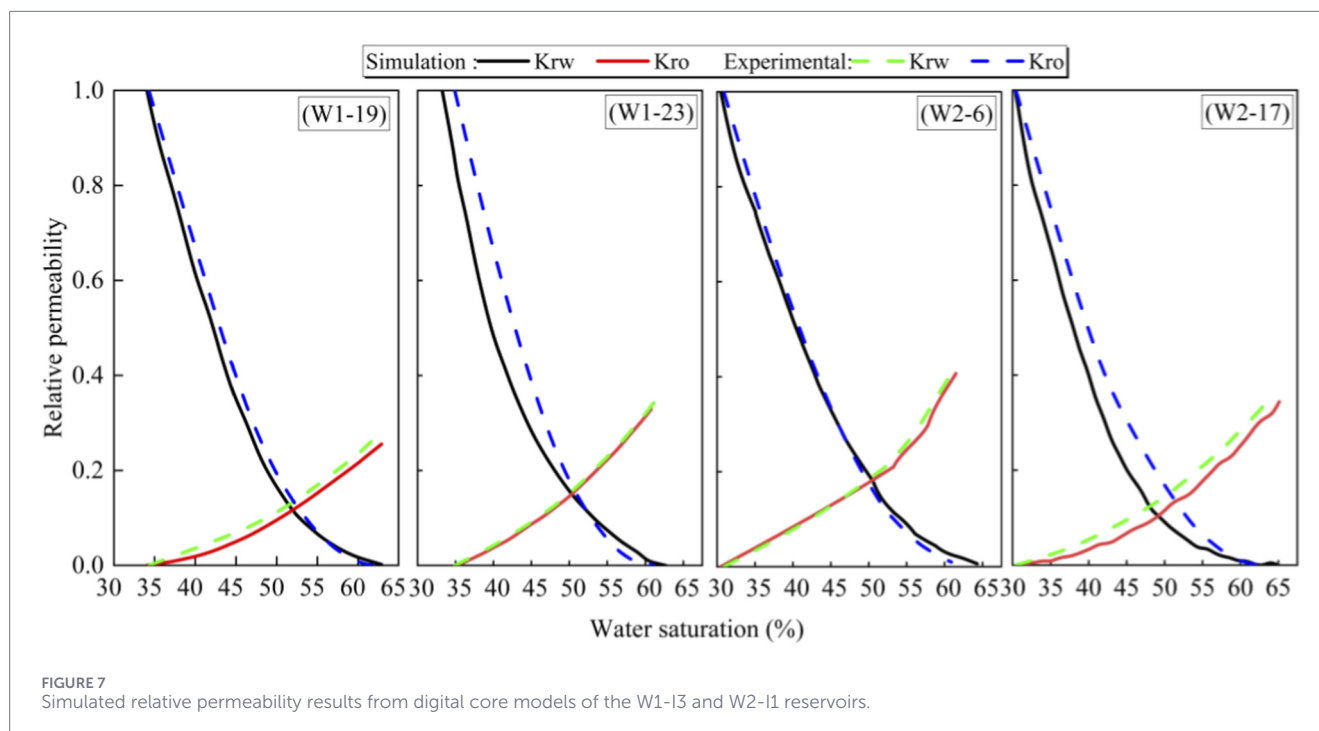
Specifically, the TPG directly characterizes the energy threshold required for fluids to overcome solid–liquid interface resistance. Experimental data indicate that when the TPG exceeds 5.0 MPa/m, it is difficult to establish an effective displacement pressure difference through conventional water flooding; thus, this parameter acts as a decisive indicator for defining effective reservoirs. Meanwhile, the throat radius represents the limiting factor restricting the seepage capacity of low-permeability reservoirs. RCMI analysis reveals a positive correlation between average throat radius and permeability. Furthermore, movable fluid saturation and permeability reflect the reservoir’s actual oil production potential and seepage efficiency, respectively. Porosity, as an indicator of storage capacity, is assigned a relatively lower weight in low-permeability media due to the influence of ineffective micro-pores.

Based on the aforementioned parameter system and combined with the distribution characteristics of measured data from the W1 and W2 blocks, the reservoirs in the target area are classified into four grades (Table 8).

Type I reservoirs represent the superior storage spaces in the study area. The lithology of these reservoirs is dominated by pebbly coarse sandstone, where feldspar grains have undergone intense secondary dissolution, forming a connected dissolution pore network. Digital rock simulation indicates a high coordination number with pore–throat connectivity exceeding 80%. In terms of seepage behavior, fluid flow is primarily controlled by inertial forces, exhibiting quasi-Darcy flow characteristics with an extremely low TPG. Due to the wide range of the oil–water two-phase co-flow region (>50%), the water flooding efficiency can exceed 60%.

Type II reservoirs are classified as potential reservoirs with moderate seepage capacity. Their pore space consists of a mixture of primary intergranular pores and dissolution pores. Affected by compaction, some large throats are compressed, with throat radii mainly distributed between 2 and 6 μm . These reservoirs exhibit weak non-linear flow characteristics; although a TPG of approximately 0.15 MPa/m exists, it can be overcome under conventional water injection pressure. Nuclear magnetic resonance (NMR) testing shows high movable fluid saturation, averaging 58.5%.

Type III reservoirs, typically represented by the W2 block, belong to the low-efficiency seepage category. The interstitial material in these reservoirs has a high content of clay minerals such as illite, with effective throat radii ranging from 1 to 2 μm . Consequently, these reservoirs exhibit significant non-linear flow characteristics and strong stress sensitivity. The TPG increases substantially to 1.8–2.5 MPa/m, indicating severe boundary layer effects under low-velocity flow. It is difficult to establish an effective



displacement system in Type III reservoirs using conventional water injection, and fingering phenomena are prone to occur.

Type IV reservoirs represent difficult-to-mobilize resources, primarily composed of zones with strong calcareous cementation or extremely fine-grained sedimentary rocks. The pore-throat system is dominated by nano-scale intercrystalline pores, with throat radii generally less than $1\ \mu\text{m}$, falling into the category of typical tight reservoirs. Fluid flow in such media is extremely difficult; the TPG is usually greater than $5.0\ \text{MPa/m}$ and can reach as high as $16.7\ \text{MPa/m}$. Most fluids are bound by strong capillary forces and surface adsorption forces, remaining in an immobile state.

5.2 Reservoir classification of the study area

Based on the comprehensive classification and evaluation system constructed above, this study integrates macroscopic physical properties and microscopic experimental data to classify the reservoirs in the target area into four grades. To clarify the specific characteristics and mobilization potential of reservoirs at different grades, this section focuses on elucidating the differences in pore-throat topological structures, mineral compositions, and non-linear flow behaviors of each reservoir type, aiming to provide a basis for reservoir quality evaluation and the formulation of development strategies.

The W1 Block Type I reservoir is characterised by a lithology comprising conglomerate and gravelly sandstone (Table 9). The core porosity of the reservoir ranges from 16% to 17%, with permeability values ranging from 10 to 50 mD. The pore types observed include dissolution pores and grain-edge fractures. The average pore radius ranges from $76\ \mu\text{m}$ to $190\ \mu\text{m}$, and the average throat radius ranges from $6\ \mu\text{m}$ to $10\ \mu\text{m}$. The pore throat coordination number varies between 3.8 and 5, indicating a relatively well-developed reservoir.

The reservoir under consideration is of type II, with a conglomerate lithology. The pore types observed were intergranular dissolution pores and grain-edge fractures. The reservoir properties were found to be satisfactory, with a core porosity of 11%–16% and a permeability of 2 mD–6 mD. Mercury porosimetry yielded a capillary pressure curve with a steep slope, and the displacement pressure was found to be less than 0. The initial findings indicate an average throat diameter of the pores greater than $5\ \mu\text{m}$, with a reservoir mobile fluid saturation level of 39% and a reservoir TPG of $0.02\ \text{MPa/m}$. In the reservoir's phase permeability test, the oil displacement efficiency is 44.6%. The average pore radius was measured to be $52\ \mu\text{m}$, the average throat radius was $6.4\ \mu\text{m}$, and the pore throat coordination number was found to be 3.4, indicating that the reservoir is of good quality.

Type III reservoir, with lithology consisting of gravel-bearing medium to coarse sandstone, and pore types including intergranular dissolution pores and grain-edge fractures. The reservoir properties are good, with core porosity ranging from 15% to 17% and permeability from 2 mD to 6 mD. Mercury porosimetry experiments yielded a capillary pressure curve with a steep slope, and displacement pressure ranging from 0.2 to 0.4 MPa. The average throat diameter of the pores is greater than $1\ \mu\text{m}$ – $4\ \mu\text{m}$. The reservoir's mobile fluid saturation is 34%–43%, and the reservoir's starting pressure gradient is 1.8–2.5 MPa/m. In the reservoir's phase permeability test, the oil displacement efficiency is 45%–53%. The average pore radius is $80\ \mu\text{m}$, the average throat radius is $4.5\ \mu\text{m}$, and the pore throat coordination number is 2.9, indicating poor reservoir quality.

Type IV reservoir, lithology consists of fine sandstone and gravelly fine sandstone, pore types include intergranular dissolution pores and grain-edge fractures, reservoir properties are poor, core porosity ranges from 3% to 13%, permeability is less than 0.5 mD, mercury porosimetry experiments yielded a capillary force curve

TABLE 7 Summary of constant-rate mercury injection test data in the study area.

Sample ID	Permeability, mD	Mean throat radius $\gamma_t/\mu\text{m}$	Mean pore radius $\gamma_p/\mu\text{m}$	Main throat radius $R_M/\mu\text{m}$	Max connected throat radius $R_{\text{max}}/\mu\text{m}$	Displacement pressure P_d/MPa	Final Hg saturation $S_r/\%$	Relative sorting coefficient D_r	Tortuosity λ
W1-19	1.56	4.056	143.997	1.500	2.952	0.249	45.020	0.714	5.119
W1-23	4.59	5.089	137.350	1.500	4.482	0.164	44.256	0.549	2.981
W1-26	0.53	1.124	149.750	0.800	1.950	0.377	53.167	2.061	7.593
W1-29	0.43	1.579	142.412	0.800	1.801	0.408	30.513	0.312	3.615
W1-35	0.08	0.428	146.534	0.400	0.920	0.799	46.214	1.361	18.482
W2-2	1.7	1.196	144.705	0.800	3.050	0.241	47.591	1.451	3.801
W2-6	2.78	1.635	147.076	1.000	3.693	0.199	64.360	1.169	4.710
W2-7	0.15	0.587	149.396	0.533	1.201	0.612	53.554	2.764	11.554
W2-10	0.58	2.042	140.882	1.400	2.014	0.365	49.212	1.058	7.886
W2-14	0.17	0.532	142.077	0.500	1.246	0.590	67.571	3.334	14.961
W2-17	2.59	1.504	143.616	0.800	3.585	0.205	59.932	0.872	4.504

with a gentle slope, and displacement pressure is approximately 0.4 MPa. The average throat size of the pores is 0.4 μm –1.5 μm , the reservoir’s mobile fluid saturation is 15%–57%, and the reservoir’s TPG is greater than 6.8 MPa/m. In phase permeability tests, the oil displacement efficiency is 41%–52%, and the reservoir quality is poor.

The reservoir in question is of the W2 Block II-type, with a lithology consisting of medium to coarse sandstone, and a porosity that includes intergranular dissolution pores and grain-edge fractures (Table 10). The reservoir properties are satisfactory, with core porosity ranging from 13% to 15% and permeability between 2 mD and 3 mD. Mercury porosimetry experiments yielded a capillary pressure curve with a gentle slope, and displacement pressure of approximately 0.2–0.3 MPa. The mean diameter of the pores’ throats is between 1.2 and 2 μm . The reservoir’s mobile fluid saturation has been measured at 58.5%, and the reservoir’s initial pressure gradient has been determined to be 0.15 MPa/m. In the reservoir’s phase permeability test, the oil displacement efficiency was found to be 52.5%. The average pore radius was measured to be between 55 and 56 μm , the average throat radius was between 4.5 and 5.5 μm , and the pore throat coordination number was between 3.5 and 6. This indicates that the reservoir is of good quality.

The reservoir in question is of Type III, with a lithology comprising gravel, sandstone, and coarse sandstone with gravel. The pore types are intergranular dissolution pores and grain-edge fractures. The reservoir properties are suboptimal, with core porosity ranging from 11.5% to 14% and permeability ranging from 0.5 mD to 2 mD. Mercury porosimetry experiments yielded a capillary force curve with a gentle slope. Displacement pressure was found to be approximately 0.2 MPa, the average throat diameter of the pores was greater than 1.6 μm , the reservoir’s mobile fluid saturation was 44%–55%, the reservoir’s TPG was 0.2–5 MPa/m, and in reservoir phase permeability tests, the oil displacement efficiency was 45%–52%. The average pore radius was found to be 64 μm , the average throat radius was 2.2 μm , and the pore throat coordination number was 3.3, indicating poor reservoir quality.

The lithology of the Type IV reservoir is composed of fine sandstone and gravelly fine sandstone. The pore types present include intergranular dissolution pores and grain-edge fractures. The reservoir properties are characterised as poor, with core porosity ranging from 10% to 13% and permeability less than 0.5 mD. Mercury porosimetry yielded a capillary force curve with a gentle slope, and displacement pressure is approximately 0.6 MPa. The average throat size of the pores is less than 0.6 μm , the reservoir’s mobile fluid saturation is less than 45%, the reservoir’s starting pressure gradient is greater than 5 MPa/m, and in phase permeability tests, the oil displacement efficiency is less than 45%.

Based on the established reservoir classification and the revealed flow mechanisms, differentiated development strategies are proposed to enhance recovery efficiency. For Type I and Type II reservoirs, which exhibit quasi-Darcy flow and good connectivity, a strategy of mild water injection with optimized well patterns is recommended to maintain formation energy and avoid fingering caused by excessive injection pressure.

For Type III reservoirs, the primary challenge lies in the high TPG induced by clay mineral hydration and boundary layer effects. Therefore, standard water flooding is inefficient. It is suggested to incorporate surfactant flooding or anti-swelling agents into the

TABLE 8 Quantitative classification standards for low-permeability reservoirs in the study area.

Classification	Flow capacity	Permeability/ mD	Mean throat radius $\gamma t/\mu\text{m}$	TPG/ MPa/m	Movable fluid sat. %	Geological characteristics
Type I	High efficiency	>10	>6.0	<0.05	>60	Massive conglomerate/coarse sandstone with strong dissolution; well-connected pore network
Type II	Medium efficiency	2.0–10	2.0–6.0	0.05–0.5	50–60	Medium sandstone; mixed pores (dissolution + residual intergranular); moderate sorting
Type III	Low efficiency	0.5–2.0	1.0–2.0	0.5–5.0	40–50	Fine-medium sandstone; clay-filling dominant; high tortuosity; threshold pressure evident
Type IV	Ineffective/Hard to produce	<0.5	<1.0	>5.0	<40	Siltstone/argillaceous sandstone; strong cementation or compaction; nano-scale throats

TABLE 9 Petrophysical parameters and digital core models of four reservoir classes in W1-I3.

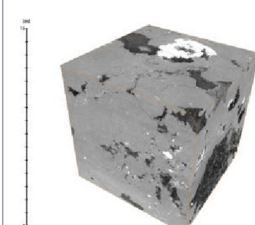
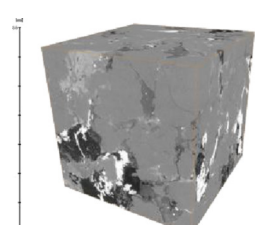
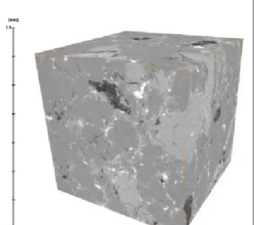

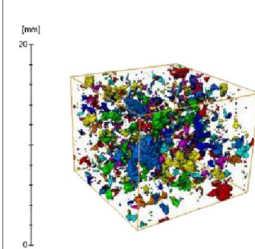
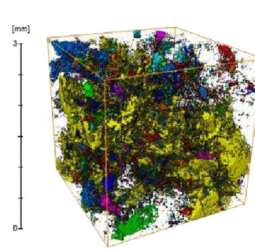
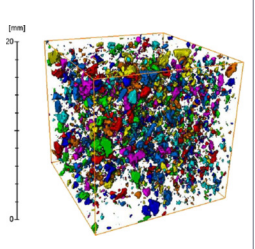
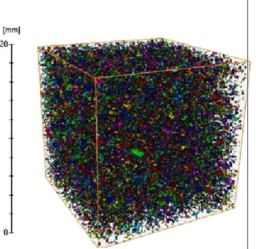
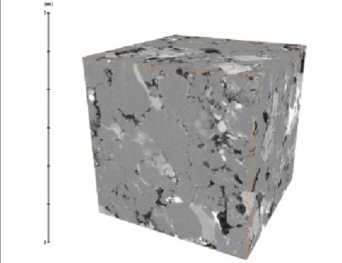
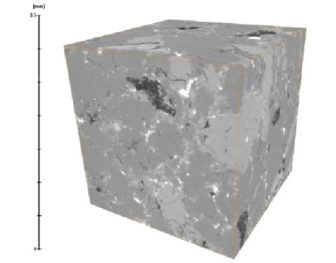
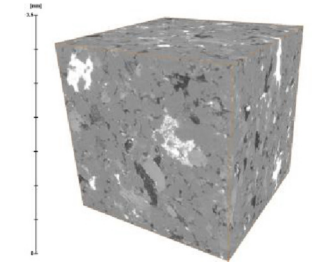
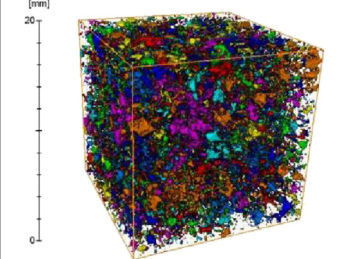
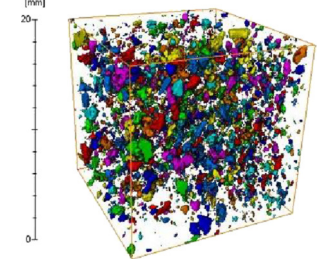
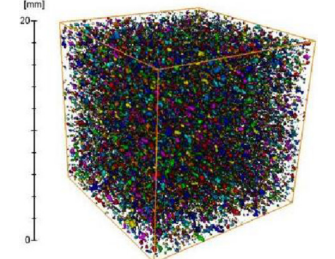
Type	I	II	III	IV
Permeability/mD	>10	1.21	5.37	<1
Porosity/%	16–17	16.50	9.50	4.10
Lithology	Conglomerate, gravelly coarse sandstone	Conglomerate	Coarse sandstone	Gravelly coarse sandstone
Digital core pore Radius/ μm	76–190	79.90	21.50	-
Digital core throat Radius/ μm	6–10	6.40	4.50	-
Pore throat coordination number	3.8–5	3.40	2.90	-
MCT image				
Pore model				

TABLE 10 Petrophysical parameters and digital core models of four reservoir classes in W2-I1.

Type	II	III	IV
Permeability/mD	2.66	1.90	<0.5
Porosity/%	13.30	11.80	12.30
Lithology	Medium-grained sandstone	Medium-coarse sandstone	Gravelly fine sandstone
Digital core pore Radius/ μm	55.50	64.40	-
Digital core throat Radius/ μm	4.70	2.20	-
Pore throat coordination number	5.80	3.40	-
MCT image			
Pore model			

injection fluid. These additives can reduce the interfacial tension at the solid–liquid interface and thin the hydration boundary layer, effectively enlarging the effective flow radius and reducing the TPG. Additionally, advanced water injection (pressurizing before production) is advised to overcome the initial flow resistance.

For Type IV reservoirs, which are currently difficult to mobilize due to nano-scale throats and TPG >5.0 MPa/m, conventional displacement methods are ineffective. Future development should rely on horizontal wells combined with multi-stage hydraulic fracturing to create artificial fracture networks that connect isolated micro-pores, turning non-movable reserves into producible assets.

6 Conclusion

1. This study elucidates that the non-linear flow capacity of low-permeability reservoirs is governed by a competitive coupling mechanism between microscopic pore–throat topology and physico-chemical boundary layer effects, rather than pore size alone. The specific “wide-pore, narrow-throat” configuration creates a fundamental geometric bottleneck, while high clay content induces thickened hydration films that further compress the effective flow radius. This synthesis explains the high porosity but low permeability paradox often observed in such reservoirs: geometric tortuosity amplifies the Jamin effect, making throat connectivity and mineral-induced surface

adsorption the primary determinants of the non-linear flow sensitivity.

2. We demonstrated that a multi-scale complementarity workflow integrating RCMI, NMR, and digital rock physics can effectively bridge the gap between static pore structure and dynamic seepage behavior, while explicitly mitigating the resolution limits and model assumptions inherent in single-scale techniques. Unlike traditional single-factor analyses, this integrated approach allows for the quantification of elusive topological parameters. The high consistency achieved between LBM simulations and physical experiments validates digital rock technology as a reliable tool for predicting relative permeability curves.
3. The establishment of the Seepage Capacity Priority classification system provides a theoretical basis for moving beyond traditional porosity-based reservoir evaluation. By explicitly incorporating dynamic parameters into the evaluation standard, this study offers a roadmap for differentiated development strategies. The findings suggest that efficient recovery of low-permeability reserves requires tailoring stimulation techniques to specific reservoir classes—ranging from mild water injection for dominantly connected reservoirs (Type I/II) to surfactant-assisted pressure boosting for high-TPG reservoirs (Type III) and volume fracturing for tight zones (Type IV)—thereby maximizing the mobilization of difficult-to-produce

Data availability statement

The raw data supporting the conclusions of this article will be made available by the authors, without undue reservation.

Author contributions

QJ: Writing – review and editing, Writing – original draft.

Funding

The author(s) declared that financial support was not received for this work and/or its publication.

Conflict of interest

The author(s) declared that this work was conducted in the absence of any commercial or financial relationships that could be construed as a potential conflict of interest.

References

- Berg, S., Dijk, H., Unsal, E., Hofmann, R., Zhao, B., and Raju Ahuja, V. (2024). Simultaneous determination of relative permeability and capillary pressure from an unsteady-state core flooding experiment?. *Comput. Geotechnics* 168, 106091. doi:10.1016/j.compgeo.2024.106091
- Cheng, H., Wang, F., Li, S., Cheng, Z., Yuan, Y., and Feng, G. (2024). From pre-darcy flow to darcy flow in porous media: a simple unified model. *Water Resour. Res.* 60, e2023WR036902. doi:10.1029/2023wr036902
- Chi, P., Sun, J., Yan, W., and Luo, X. (2024). Multiscale fusion of tight sandstone digital rocks using attention-guided generative adversarial network. *Mar. Petroleum Geol.* 160, 106647. doi:10.1016/j.marpetgeo.2023.106647
- Fan, J., Guo, W., Lv, Y., Jiang, T., Zhu, Y., and Liu, L. (2023). A nonlinear mathematical model for fluid flow in low-permeability reservoirs and its effect on well production performance. *Geoenergy Sci. Eng.* 231, 212349. doi:10.1016/j.geoen.2023.212349
- Faramarzi-Palanger, M., and Mirzaei-Paiaman, A. (2021). Investigating dynamic rock quality in two-phase flow systems using TEM-function: a comparative study of different rock typing indices. *Petroleum Res.* 6, 16–25. doi:10.1016/j.ptlrs.2020.08.001
- Gong, J., and Bai, Y. (2024). Characterization of microscopic pore structure in tight sandstone reservoir: a case study of yanchang formation in southeastern ordos basin. *Geol. Resour.* 33 (5), 662–670. doi:10.13686/j.cnki.dzyzy.2024.05.006
- Guo, C., Qin, Y., and Yang, Z. B. (2014). Coal reservoirs NMR T2 spectrum and gas-water relative permeability characteristics and their controlling factors in bidu-santang basin, Western Guizhou. *J. China Univ. Min. Technol.* 43, 841–852.
- Huang, H., Tan, J., He, Y., Tang, C., Yang, B., Hu, Z., et al. (2022). Quantitative characterization of pore structure and evaluation and prediction on low porosity and low permeability reservoirs. *Coal Technol.* 41, 94–96. doi:10.13301/j.cnki.ct.2022.10.022
- Jia, L., Zhong, L., Wang, G., Hu, C., Gong, Y., Shang, C., et al. (2024). Flow law and liquid resistance effect of water-in-oil emulsion in porous media. *Oilfield Chem.* 41 (4), 664–670. doi:10.19346/j.cnki.1000-4092.2024.04.013
- Lai, J., Xiao, L., Zhao, X., Zhao, F., Li, Y., Zhu, S., et al. (2023). Genesis and logging evaluation of deep to ultra-deep high-quality clastic reservoirs: a case study of the Cretaceous bashijiqike formation in kuqa depression. *Acta Pet. Sin.* 44, 612–625. doi:10.7623/syxb202304004
- Li, M., Guo, Y., and Yang, Y. (2023). Effects of clay minerals and pore-throat characteristics on the movable fluid of tight sandstones: a case study of the Shanxi formation in eastern ordos basin. *Nat. Gas. Geosci.* 34, 1627–1640. doi:10.11764/j.issn.1672-1926.2023.04.004
- Lin, H., Zhang, W., Guo, S., Zhang, X., Wang, L., and Zhang, J. (2025). Study on the energy evolution mechanism and fractal characteristics of coal failure under dynamic loading. *ACS Omega* 10, 54710–54719. doi:10.1021/acsomega.5c08162

Generative AI statement

The author(s) declared that generative AI was not used in the creation of this manuscript.

Any alternative text (alt text) provided alongside figures in this article has been generated by Frontiers with the support of artificial intelligence and reasonable efforts have been made to ensure accuracy, including review by the authors wherever possible. If you identify any issues, please contact us.

Publisher's note

All claims expressed in this article are solely those of the authors and do not necessarily represent those of their affiliated organizations, or those of the publisher, the editors and the reviewers. Any product that may be evaluated in this article, or claim that may be made by its manufacturer, is not guaranteed or endorsed by the publisher.

- Nabipour, I., Raoof, A., Cnudde, V., Aghaei, H., and Qajar, J. (2024). A computationally efficient modeling of flow in complex porous media by coupling multiscale digital rock physics and deep learning: improving the tradeoff between resolution and field-of-view. *Adv. Water Resour.* 188, 104695. doi:10.1016/j.advwatres.2024.104695
- Wang, L., Li, X., Wang, J., Zhang, H., Shi, H., Liu, G., et al. (2025). Effect of pore-throat structure on irreducible water saturation and gas seepage capacity in a multilayer tight sandstone gas reservoir. *Geoenergy Sci. Eng.* 249, 213787. doi:10.1016/j.geoen.2025.213787
- Wu, H. K., Cao, K., and Zhao, F. F. (2021). NMR experimental study of movable fluid saturation in low permeability sedimentary rocks. *Nat. Gas. Geosci.* 32, 457–463. doi:10.11764/j.issn.1672-1926.2020.09.011
- Yue, Y., Yidi, S., Rui, G., Lina, D., Jingwei, H., and Mi, Y. (2022). Determination of surface relaxivity for tight sandstone cores based on T2 cut-off value. *Petroleum Geol. & Exp.* 44, 342–349. doi:10.11781/sydz202202342
- Yunlong, J., Zhengzheng, C., Zhenhua, L., Feng, D., Cunhan, H., Haixiao, L., et al. (2024). Nonlinear evolution characteristics and seepage mechanical model of fluids in broken rock mass based on the bifurcation theory. *Sci. Rep.* 14, 10982. doi:10.1038/s41598-024-61968-6
- Zhang, X., Du, H. L., Ding, C., Liu, H. X., and Mu, Z. J. (2017). "The factors of threshold pressure gradient for CO₂ Miscible flooding in low permeability reservoir," in *3rd 2017 international conference on sustainable development (ICSD 2017)* (Tianjin: Atlantis Press), 38–44. doi:10.2991/ICSD-17.2017.6
- Zhang, X., Zhang, J., Yuan, J., Cui, X., and Mao, Z. (2021). Micro pore throat structure and its influence on seepage of Chang81 tight reservoir in Nanliang-Huachi area, Ordos Basin. *Lithol. Reserv.* 33, 36–48. doi:10.12108/xyyqc.20210205
- Zhang, X., Wei, L., Wan, H., Hao, M., and Zhu, J. (2025). Research progress and application of low permeability reservoir characterization techniques. *Petrochem. Ind. Appl.* 44, 10–15. doi:10.3969/j.issn.1673-5285.2025.01.002
- Zhao, X., Liu, B., Guo, R., Zhang, S., Li, Y., and Tian, Z. (2017). Reservoir characterization and its application to development. *Petroleum Geol. & Exp.* 39, 287–294. doi:10.11781/sydz201702287
- Zhao, M., Cao, M., He, H., and Dai, C. (2020). Study on variation laws of fluid threshold pressure gradient in low permeable reservoir. *Energies* 13, 3704. doi:10.3390/en13143704
- Zhengzheng, C., Shuaiyang, Z., Zhenhua, L., Feng, D., Cunhan, H., and Wenqiang, W. (2024). Numerical research on disastrous mechanism of seepage instability of karst collapse column considering variable mass effect. *Sci. Rep.* 14, 13900. doi:10.1038/s41598-024-63344-w